

Learning V1 cells with vector representations of local contents and matrix representations of local motions

Ruiqi Gao

UCLA Department of Statistics
ruiqigao@ucla.edu

Jianwen Xie

Hikvision Research Institute
jianwen@ucla.edu

Song-Chun Zhu

UCLA Department of Statistics
sczhu@stat.ucla.edu

Ying Nian Wu

UCLA Department of Statistics
ywu@stat.ucla.edu

Abstract

Simple cells in primary visual cortex (V1) can be approximated by Gabor filters, and adjacent simple cells tend to have quadrature phase relationship. This paper entertains the hypothesis that a key purpose of such simple cells is to perceive local motions, i.e., displacements of pixels, caused by the relative motions between the agent and the surrounding environment. Specifically, we propose a representational model that couples the vector representations of local image contents with the matrix representations of local pixel displacements. When the image changes from one time frame to the next due to pixel displacements, the vector at each pixel is rotated by a matrix that represents the displacement of this pixel. We show that by learning from pair of images that are deformed versions of each other, we can learn both vector and matrix representations. The units in the learned vector representations reproduce properties of V1 simple cells. The learned model enables perceptual inference of local motions.

1 Introduction

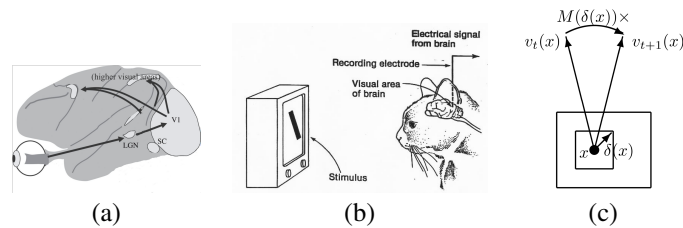


Figure 1: (a) Primary visual cortex or V1 is the first step in representing and interpreting retina image data (source: internet). (b) Cells in V1 respond to bars of different locations, orientations and sizes (source: internet). (c) Vector representations of local image contents and matrix representations of local pixel displacements.

David Hubel and Torsten Wiesel won the Nobel Prize for Physiology or Medicine in 1981 for their discovery of simple and complex cells in the primary visual cortex or V1 [10]. Figure 1(a) illustrates the V1 area. Hubel and Wiesel discovered that cells in V1 of the cat brain responded to bars of different locations, orientations and scales, and each cell responded to a bar at a particular location, orientation and scale. See Figure 1(b). Some V1 cells are called simple cells, which behave like linear filters. A mathematical model of a simple cell is Gabor filter [5], which is sine or cosine plane

wave multiplied by an elongate Gaussian function. It was observed that adjacent simple cells have quadrature phase relationship [25], i.e., the phases of their sine waves differ by $\pi/2$, such as a Gabor sine filter and a Gabor cosine filter. A complex cell can be modeled by the sum of squares of the responses from a pair of simple cells of quadrature phases. The goal of this paper is to understand the mathematical principle and model underlying such V1 cells.

We entertain the hypothesis that a key purpose of the V1 cells is to perceive local motions, i.e., displacements of pixels, caused by the relative motions between the agent and the surrounding 3D environment. We propose a representational model that couples the vector representation of static image contents with the matrix representation of changes due to pixel displacements. See Figure 1(c) an illustration, where the image is illustrated by the big rectangle. A pixel is illustrated by a dot. The local image content is illustrated by a small square around it. The displacement of the pixel is illustrated by a short arrow, which is within the small square. The vector representation of the local image content is represented by a long vector, which rotates as the image undergoes change due to the pixel displacements. See Section 3 for a detailed explanation of the mathematical notation in this figure.

Our model consists of the following two parts:

- (1) Vector representation of local image content. The local content around each pixel is represented by a high dimensional vector. Each unit in the vector is obtained by a linear filter. These local filters or wavelets are assumed to form a tight frame, i.e., the image can be reconstructed from the vectors using the linear filters as the basis functions.
- (2) Matrix representation of local displacement. The change of the image from the current time frame to the next time frame is caused by the displacements of the pixels. Each possible displacement is represented by a matrix that acts on the vector. When the image changes according to the displacements, the vector at each pixel is multiplied by the matrix that represents the local displacement, in other words, the vector at each pixel is rotated by the matrix representation of the displacement of this pixel.

We train this representational model on image pairs where in each pair, the second image is a deformed version of the first image, and the deformation is known. We learn the encoding matrices for vector representation and the matrices that represent the pixel displacements from the training data. Our experiments show that our method can learn V1-like units that can be well approximated by Gabor filters with quadrature phase relationship. After learning the encoding matrices for vector representation and the matrix representations of the displacements, we can infer the displacement fields using the learned model.

2 Contributions and related work

This paper proposes a simple representational model that couples the vector representations of image contents and matrix representations of local pixel displacements. The model is new and different from existing models for V1. The learned units resemble V1 simple cells. The learned model is capable of inferring local motions.

Most well known models for V1 cells are concerned with statistical properties of natural images or video sequences. Examples include sparse coding model [23, 18, 21], independent component analysis (ICA) [12, 3, 30], slowness criterion [11, 31], and prediction [29]. While these models are very compelling, they do not serve a direct purpose of perceptual inference. Our model is learned for the direct purpose of perceiving local motions caused by relative motion between the agent and the surrounding 3D environment. This is crucial for the survival of the agent as a predator or a prey, and it enables reconstruction of 3D environment via shape from motion. Our model also gives a natural explanation of quadrature phase relationship between adjacent simple cells [25].

3 Representational model

3.1 Vector representation

Let $(\mathbf{I}(x), x \in D)$ be an image observed at a certain instant, where $x = (x_1, x_2) \in D$ is the 2D coordinates of pixel. D is the image domain (e.g., 128×128). We represent the image \mathbf{I} by

vectors $(v(x), x \in D_-)$, where each $v(x)$ is a vector defined at pixel x , and D_- may consist of a sub-sampled set of pixels in D (e.g., sub-sampled every 8 pixels). $V = (v(x), x \in D_-)$ forms a vector representation of the whole image.

We assume the vector encoding is linear and convolutional. Specifically, let $\mathbf{I}[x]$ be a squared patch (e.g., 16×16) of \mathbf{I} centered at x . We can make $\mathbf{I}[x]$ into a vector (e.g., 256 dimensional). Let

$$v(x) = \mathbf{W}\mathbf{I}[x], x \in D_-, \quad (1)$$

be the linear encoder, where W is the encoding matrix that encodes $\mathbf{I}[x]$ into a vector $v(x)$, and W is the same for all x , i.e., convolutional. The rows of W are the linear filters and can be displayed as local image patches of the same size as the image patch $\mathbf{I}[x]$. We can write $V = \mathbf{W}\mathbf{I}$, if we treat \mathbf{I} as a vector, and the rows of \mathbf{W} are the shifted or translated versions of W .

3.2 Tight frame and isometry

We assume that \mathbf{W} is an auto-encoding tight frame, i.e., $\mathbf{I} = \mathbf{W}^\top V$, i.e.,

$$\mathbf{I} = \sum_{x \in D_-} W^\top v(x). \quad (2)$$

Thus, each row of W serves as a linear filter for bottom-up encoding, as well as a basis function for top-down decoding. Both the encoder and decoder can be implemented by convolutional linear neural networks.

The tight frame assumption can be justified by the fact that for two images \mathbf{I} and \mathbf{J} , we have $\langle \mathbf{W}\mathbf{I}, \mathbf{W}\mathbf{J} \rangle = \mathbf{I}^\top \mathbf{W}^\top \mathbf{W}\mathbf{J} = \langle \mathbf{I}, \mathbf{J} \rangle$, that is, the vector representation preserves the inner product, i.e., the representation has the isometry property. As a result, $\|\mathbf{W}\mathbf{I}\| = \|\mathbf{I}\|$, $\|\mathbf{W}\mathbf{J}\| = \|\mathbf{J}\|$, thus the vector representation also preserves the angle.

Thus when the image \mathbf{I} changes from \mathbf{I}_t to \mathbf{I}_{t+1} , its vector representation V also changes from V_t to V_{t+1} , and the angle between \mathbf{I}_t and \mathbf{I}_{t+1} is the same as the angle between V_t and V_{t+1} .

3.3 Sub-vectors

The vector $v(x)$ can be high-dimensional. We further divide $v(x)$ into K sub-vectors, $v(x) = (v^{(k)}(x), k = 1, \dots, K)$. Each sub-vector is obtained by an encoding sub-matrix $W^{(k)}$, i.e., $v^{(k)}(x) = W^{(k)}\mathbf{I}[x]$, $k = 1, \dots, K$, where $W^{(k)}$ consists of the rows of W that correspond to $v^{(k)}$. According to the tight frame assumption, we have $\mathbf{I} = \sum_{x \in D_-} \sum_{k=1}^K W^{(k)\top} v^{(k)}(x)$.

3.4 Matrix representation

Let \mathbf{I}_t be the image at time frame t . Suppose the pixels of \mathbf{I}_t undergo local displacements, where the displacement at pixel x is $\delta(x)$. We assume that $\delta(x)$ is within a squared range Δ (e.g., $[-6, 6] \times [-6, 6]$ pixels) that is inside the range of $\mathbf{I}_t[x]$ (e.g., 16×16 pixels). Let \mathbf{I}_{t+1} be the resulting image. Let $v_t(x)$ be the vector representation of $\mathbf{I}_t[x]$, and let $v_{t+1}(x)$ be the vector representation of $\mathbf{I}_{t+1}[x]$. Then $v_t(x) = (v_t^{(k)}(x), k = 1, \dots, K)$, and $v_{t+1}(x) = (v_{t+1}^{(k)}(x), k = 1, \dots, K)$.

The transition from \mathbf{I}_t to \mathbf{I}_{t+1} is illustrated by the following diagram:

$$\begin{array}{ccc} v_t^{(k)}(x) & \xrightarrow{M^{(k)}(\delta(x)) \times} & v_{t+1}^{(k)}(x) \\ W^{(k)} \uparrow & & \uparrow W^{(k)} \\ \mathbf{I}_t & \xrightarrow{\delta(x)} & \mathbf{I}_{t+1} \end{array} \quad (3)$$

Specifically, we assume that

$$v_{t+1}^{(k)}(x) = M^{(k)}(\delta(x))v_t^{(k)}(x), \forall x \in D_-, k = 1, \dots, K. \quad (4)$$

That is, when \mathbf{I} changes from \mathbf{I}_t to \mathbf{I}_{t+1} , $v^{(k)}(x)$ undergoes a linear transformation, driven by a matrix $M^{(k)}(\delta(x))$, which depends on the local displacement $\delta(x)$. In terms of the whole vector $v(x) = (v^{(k)}(x), k = 1, \dots, K)$, we have $v_{t+1}(x) = M(\delta(x))v_t(x)$, where $M(\delta(x)) = \text{diag}(M^{(k)}(\delta(x)), k = 1, \dots, K)$ is the matrix representation of the local displacement $\delta(x)$.

3.5 Disentangled rotations

The linear transformations of the sub-vectors $v^{(k)}(x)$ can be considered as rotations. Here we use the word ‘‘rotation’’ in the loose sense without strictly enforcing $M^{(k)}(\delta)$ to be orthogonal. $v(x)$ is like a multi-arm clock, with each arm $v^{(k)}(x)$ rotated by $M^{(k)}(\delta(x))$. The rotations of $v^{(k)}(x)$ for different k and x are disentangled. Here disentanglement means that the rotation of a sub-vector does not depend on other sub-vectors.

The disentanglement between different positions x is the key feature of our model. Recall the change of image \mathbf{I} is caused by the displacement of pixels, yet the rotations of sub-vectors $v^{(k)}(x)$ at different pixels x are disentangled. This enables the agent to sense the displacement of a pixel only by sensing the rotations of the sub-vectors at this pixel without linking pixels of consecutive frames.

3.6 Parametrization

We can discretize the displacement $\delta(x)$ into a finite set of possible values $\{\delta\}$, and we learn a separate $M^{(k)}(\delta)$ for each δ . We can also learn a parametric version of $M^{(k)}(\delta)$ as the second order Taylor expansion of a matrix-valued function of $\delta = (\delta_1, \delta_2)$, $M^{(k)}(\delta) = I + B_1^{(k)}\delta_1 + B_2^{(k)}\delta_2 + B_{11}^{(k)}\delta_1^2 + B_{22}^{(k)}\delta_2^2 + B_{12}^{(k)}\delta_1\delta_2$, where I is the identity matrix, and $B^{(k)} = (B_1^{(k)}, B_2^{(k)}, B_{11}^{(k)}, B_{22}^{(k)}, B_{12}^{(k)})$ are matrices of coefficients of the same dimensionality as $M^{(k)}(\delta)$.

3.7 Local mixing

If $\delta(x)$ is large, $v_{t+1}^{(k)}(x)$ may contain information from adjacent image patches of \mathbf{I}_t in addition to $\mathbf{I}_t[x]$. We can generalize the motion model in Equation (4) to allow local mixing of encoded vectors. Let \mathcal{S} be a local support centered at 0. We assume that

$$v_{t+1}^{(k)}(x) = \sum_{dx \in \mathcal{S}} M^{(k)}(\delta(x), dx) v_t^{(k)}(x + dx) \quad (5)$$

In the learning algorithm, we discretize dx and learn a separate $M^{(k)}(\delta, dx)$ for each dx .

4 Learning and inference

The input data consists of the triplets $(\mathbf{I}_t, (\delta(x), x \in D_-), \mathbf{I}_{t+1})$, where $(\delta(x))$ is the given displacement field. The learned model consists of matrices $(W^{(k)}, M^{(k)}(\delta), k = 1, \dots, K, \delta \in \Delta)$, where Δ is the range of δ . In the case of parametric $M^{(k)}$, we learn the B matrices in the second order Taylor expansion in subsection 3.6.

4.1 Loss functions for learning

We use the following loss functions:

(1) Rotation loss

$$L_{1,x,k} = \left\| W^{(k)} \mathbf{I}_{t+1}[x] - M^{(k)}(\delta(x)) W^{(k)} \mathbf{I}_t[x] \right\|^2. \quad (6)$$

For local mixing generalization, $L_{1,x,k} = \left\| W^{(k)} \mathbf{I}_{t+1}[x] - \sum_{dx \in \mathcal{S}} M^{(k)}(\delta(x), dx) W^{(k)} \mathbf{I}_t(x + dx) \right\|^2$.

(2) Reconstruction loss

$$L_2 = \left\| \mathbf{I}_t - \sum_{x \in D_-} W^\top W \mathbf{I}_t[x] \right\|^2 + \left\| \mathbf{I}_{t+1} - \sum_{x \in D_-} W^\top W \mathbf{I}_{t+1}[x] \right\|^2. \quad (7)$$

In the learning algorithm, we learn the model by a weighted sum of the expectations of $\sum_{k=1}^K \sum_{x \in D_-} L_{1,x,k}$ and L_2 , where the expectations are taken over the training pairs of images and the corresponding displacement fields.

In addition, we may add a term $L_{3,x,k} = (\|W^{(k)} \mathbf{I}_{t+1}[x]\| - \|W^{(k)} \mathbf{I}_t[x]\|)^2$ to enforce the stability of norm. Together with $L_{1,x,k}$, it forces $M^{(k)}(\delta)$ to be close to orthogonal.

4.2 Inference of motion

After learning $(W^{(k)}, M^{(k)}(\delta), \forall k, \forall \delta)$, for a testing pair $(\mathbf{I}_t, \mathbf{I}_{t+1})$, we can infer the pixel displacement field $(\delta(x), x \in D_-)$ by minimizing the rotation loss: $\delta(x) = \arg \max_{\delta \in \Delta} L_{1,x}(\delta)$, where

$$L_{1,x}(\delta) = \sum_{k=1}^K \left\| W^{(k)} \mathbf{I}_{t+1}[x] - M^{(k)}(\delta) W^{(k)} \mathbf{I}_t[x] \right\|^2 = \|W \mathbf{I}_{t+1}[x] - M^{(k)}(\delta) W \mathbf{I}_t[x]\|^2. \quad (8)$$

This algorithm is efficient because it can be parallelized for all $x \in D_-$ and for all $\delta \in \Delta$.

If we learn a parametric model for $M^{(k)}(\delta)$, we can infer the displacement field $(\delta(x), \forall x)$ by minimizing $\sum_x L_{1,x}(\delta(x))$ using gradient descent with an initialization of $(\delta(x))$ from random small values. To encourage the smoothness of the displacement field, we can add the penalty term $\|\nabla \delta(x)\|^2$.

4.3 Biological interpretations of cells and synaptic connections

The learned $(W^{(k)}, M^{(k)}(\delta), \forall k, \delta)$ can be interpreted as synaptic connections. For each k , $W^{(k)}$ corresponds to one set of connection weights. Suppose $\delta \in \Delta$ is discretized, then for each δ , $M^{(k)}(\delta)$ corresponds to one set of connection weights, and $(M^{(k)}(\delta), \delta \in \Delta)$ corresponds to multiple sets of connection weights. After computing $v_{t,x}^{(k)} = W^{(k)} \mathbf{I}_t[x]$, $M^{(k)}(\delta) v_{t,x}^{(k)}$ is computed simultaneously for every $\delta \in \Delta$. Then $\delta(x)$ is inferred by max pooling according to Equation (8).

$v_{t,x}^{(k)}$ can be interpreted as activities of simple cells, and $\|v_{t,x}^{(k)}\|^2$ can be interpreted as activity of a complex cell. If we enforce norm stability so that $\|v_{t,x}^{(k)}\| \approx \|v_{t+1,x}^{(k)}\|$, then the complex cell response is invariant to the local motion and is related to the slowness property [11, 31], which is a by-product of our model if $M^{(k)}(\delta)$ is a rotation matrix, which is covariant with the local motion.

4.4 Spatiotemporal filters and recurrent implementation

If we enforce norm stability or the orthogonality of $M^{(k)}(\delta)$, then minimizing $\|v_{t+1,x} - M(\delta)v_{t,x}\|^2$ over $\delta \in \Delta$ is equivalent to maximizing $\langle v_{t+1,x}, M(\delta)v_{t,x} \rangle$, which in turn is equivalent to maximizing $\|v_{t+1,x} + M(\delta)v_{t,x}\|^2$ so that $v_{t+1,x}$ and $M(\delta)v_{t,x}$ are aligned. This alignment criterion can be conveniently generalized to multiple consecutive frames, so that we can estimate the velocity at x by maximizing the m -step alignment score $\|u\|^2$, where

$$u = \sum_{i=0}^m M(\delta)^{m-i} v_{t+i,x} = \sum_{i=0}^m M(\delta)^{m-i} W \mathbf{I}_{t+i}[x] \quad (9)$$

consists of responses of spatiotemporal filters, and $\|u\|^2$ corresponds to the energy of motion δ in the motion energy model [1] for direction selective cells. Thus our model leads to the motion energy model. Moreover, our model enables a recurrent network for computing u by $u_i = v_{t+i,x} + M(\delta)u_{i-1}$ for $i = 0, \dots, m$, with $u_{-1} = 0$, and $u = u_m$. This recurrent implementation is much more efficient and biologically plausible than the plain implementation of spatiotemporal filtering which requires memorizing all the \mathbf{I}_{t+i} for $i = 0, \dots, m$. See [24] for a discussion of biological plausibility of recurrent implementation of spatiotemporal filtering in general.

5 Experiments

We learn our model $(W^{(k)}, M^{(k)}(\delta), k = 1, \dots, K)$ from image pairs $(\mathbf{I}_t, (\delta(x)), \mathbf{I}_{t+1})$. The number of sub-vectors $K = 40$, and the number of units in each sub-vector $v^{(k)}(x)$ is 2. We also try other dimensionalities of sub-vector, e.g., 4 and 6. See the appendix 7.3. Each row of the encoding matrix $W^{(k)}$ is a filter. The size of the filter is 16×16 , with a sub-sampling rate of 8 pixels in order to get D_- . We learn the model using stochastic gradient descent implemented by Adam [17].

5.1 Self-supervised learning

The training data consist of $(\mathbf{I}_t, (\delta(x), \forall x \in D_-), \mathbf{I}_{t+1})$, where $(\delta(x), \forall x \in D_-)$ is the field of displacements. We obtain the training data by collecting static images for (\mathbf{I}_t) and simulate the

displacement field $(\delta(x))$. The simulated displacement field is then used to deform \mathbf{I}_t to obtain \mathbf{I}_{t+1} . We refer to this method as self-supervised learning, in the sense that we can generate displacement fields by ourselves and we have the access to the ground truth displacement fields during training. At each mini-batch iteration of training, we can randomly generate $(\delta(x))$ online, which provides us training data with diverse displacement fields.

We randomly sample natural images as \mathbf{I}_t from MIT places365 dataset [32]. The images are scaled to 128×128 . We sub-sample the pixels of images into a $m \times m$ grid ($m = 4$ in the experiments), and randomly generate displacements on the grid points, which serve as the control points for deformation. Then $\delta(x)$ for $x \in D$ can be obtained by spline interpolation of the displacements on the control points. We get \mathbf{I}_{t+1} by warping \mathbf{I}_t using $\delta(x)$ [15]. When generating a displacement $\delta = (\delta_1, \delta_2)$, both δ_1 and δ_2 are randomly sampled from a range of pixels, which is set to $[-6, +6]$.

Self-supervised learning is biologically plausible because the agent can control its self-motion and has knowledge of depth of nearby objects. It can also displace nearby objects. All these provide information for pixel displacements.

5.2 Learned Gabor-like units with quadrature phase relationship

We first learn the system on the original generated image pairs. Figure 7(a) displays the learned units, i.e., rows of $W^{(k)}$. The units are learned with non-parametric $M(\delta)$, i.e., we learn a separate $M(\delta)$ for each displacement. $\delta(x)$ is discretized with an interval of 0.5. Similar patterns can be obtained by using parametric version of $M(\delta)$. Please refer to the appendix 7.1 and 7.3 for more results, including an animation of the learned units, and filters learned with local mixing motion model (eqn. (5)) and different block sizes. V1-like patterns emerge from the learned units.

To further analyze the spatial profile of the learned units, we fit every unit by a two dimensional Gabor function[16]: $h(x', y') = A \exp(-(x'/\sqrt{2}\sigma_{x'})^2 - (y'/\sqrt{2}\sigma_{y'})^2) \cos(2\pi f x' + \phi)$, where (x', y') is obtained by translating and rotating the original coordinate system (x_0, y_0) : $x' = (x - x_0) \cos \theta + (y - y_0) \sin \theta$, $y' = -(x - x_0) \sin \theta + (y - y_0) \cos \theta$. The fitted Gabor patterns are shown in figure 7(b), with the average fitting r^2 equal to 0.96 (std = 0.04). The average spatial-frequency bandwidth is 1.13 octaves, with range of 0.12 to 4.67. Figure(c) shows the distribution of the spatial-frequency bandwidth, where the majority falls within range of 0.5 to 2.5. The characteristics are reasonably similar to those of simple-cell receptive fields in the cat [14] (weighted mean 1.32 octaves, range of 0.5 to 2.5) and the macaque monkey [8] (median 1.4 octaves, range of 0.4 to 2.6). To analyze the distribution of the spatial phase ϕ , we follow the method in [27] to transform the parameter ϕ into an effective range of 0 to $\pi/2$, and plot the histogram of the transformed ϕ in figure 7(c). The strong bimodal with phases clustering near 0 and $\pi/2$ is consistent with those of the macaque monkey [27].

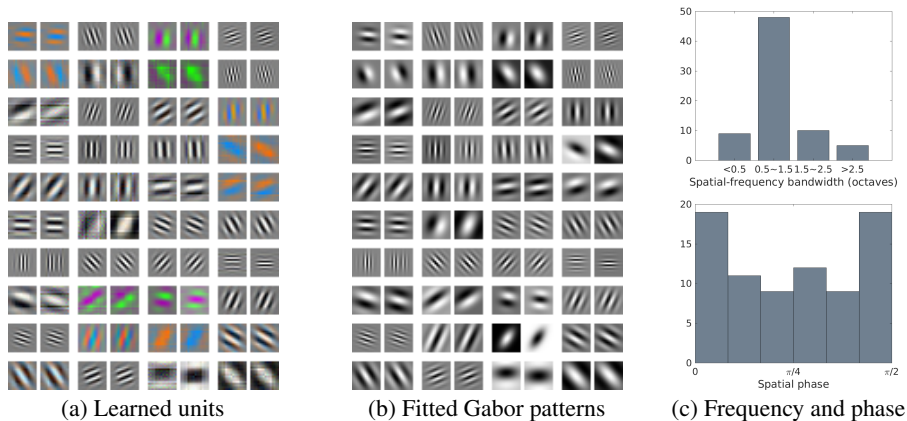


Figure 2: Learned results on the original image pairs. (a) Learned units. Each block shows two learned units within the same sub-vector. (b) Fitted Gabor patterns. (c) Distributions of spatial-frequency bandwidth (in octaves) and spatial phase ϕ .

In the above experiment, we fix the size of the convolutional filters (16×16 pixels). A more reasonable model is to have different sizes of convolutional filters, with small size filters capturing

high frequency content and big size filters capturing low frequency content. For fixed size filters, they should only account for the image content within a frequency band. To this end, we smooth every original image by two Gaussian smoothing kernels (kernel size 8, $\sigma = 1, 4$), and take the difference between the two smoothed images as the input image of the model. The effect of the two smoothing kernels is similar to a bandpass filter, so that the input images are constrained within a certain range of frequencies. The learned filters are shown in 3(a). Again for every unit, we fit it by a two dimensional Gabor function, resulting in an average fitting $r^2 = 0.83$ (std = 0.12). Following the analysis of [27, 26], a scatter plot of $n_x = \sigma_x f$ versus $n_y = \sigma_y f$ is constructed in Figure 3(b) based on the fitted parameters, where n_x and n_y represent the width and length of the Gabor envelopes measured in periods of the cosine waves. Compared to Sparsenet [22, 23], the learned units by our model have more similar structure to the receptive fields of macaque monkey.

We also show profile of the learned units within each sub-vector in Figure 3(c). Within each sub-vector, the frequency f and orientation θ of the paired units tends to be the same. More importantly, most of the paired units differ in phase ϕ by approximately $\pi/2$, consistent with the quadratic phase relationship between adjacent simple cells [25, 7].

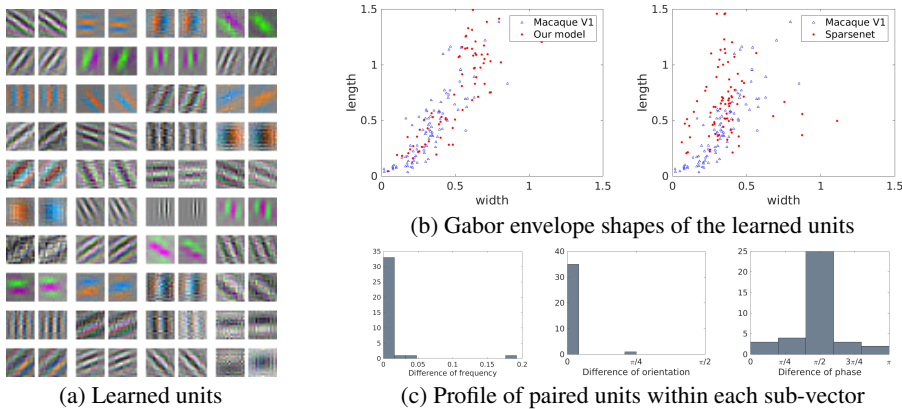


Figure 3: Learned results on band-pass image pairs. (a) Learned units. Each block shows two learned units within the same sub-vector. (b) Distribution of the Gabor envelope shapes in the width and length plane. (c) Difference of frequency f , orientation θ and phase ϕ of paired units within each sub-vector.

5.3 Inference of displacement field

We then test the learned representations in terms of inferring the displacement field ($\delta(x)$) between pairs of frames ($\mathbf{I}_t, \mathbf{I}_{t+1}$). To make fair comparison with other methods, we generate 20,000 image pairs ($\mathbf{I}_t, \mathbf{I}_{t+1}$) and the corresponding displacement field ($\delta(x)$) for training, instead of generating ($\delta(x)$) online at each iteration. Then another 3,000 image pairs are generated for testing. To get valid image patches for the inference, we leave out those displacements at image border (8 pixels at each side). Figure 9 displays several examples of the inferred displacement field, learned with non-parametric $M(\delta)$, using either the original motion model (eqn. (4)) or the local mixing motion model (eqn. (5)), where the local support \mathcal{S} is in a range of $[-4, +4]$, and dx is taken with a sub-sampling rate of 2. The inference is improved by introducing local mixing. We compute the average distance between the inferred and ground truth displacements under the two settings, which is summarized in Table 1. We also compare with some baseline methods, such as the FlowNet and its variants [6, 13]. Those methods train deep and complicated neural networks to predict optical flows in supervised manners. See appendix 7.4 for the qualitative comparison with those methods.

Table 1: Average distance between inferred and ground truth displacements (FN stands for FlowNet)

methods	FNC	FNS	FNSD	FNCS	FN2	Ours (no-mixing)	Ours (local mixing)
Inference error	1.324	1.316	0.799	0.713	0.686	0.884	0.444

We did not use existing optical flow datasets [6, 4, 9, 20] for supervised learning because those datasets, which are also simulated, contain motions that tend to be too large for our model which

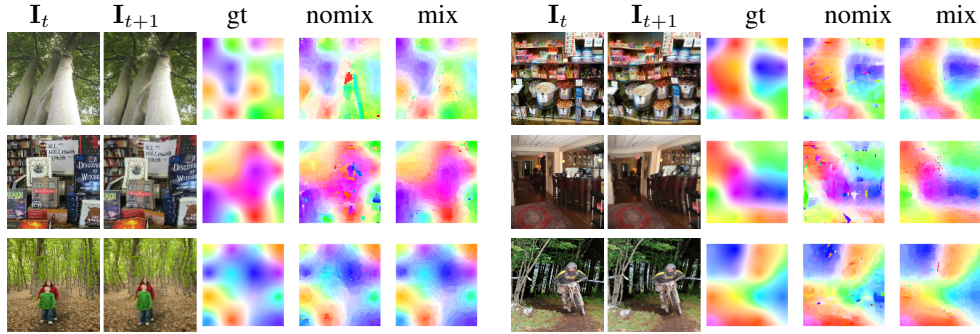


Figure 4: Examples of inference of displacement field. For each block, from left to right are I_t , I_{t+1} , ground truth displacement field and inferred displacement field with the original motion model and local mixing motion model respectively. The displacement fields are color coded. See appendix 7.2 for the color code [19].

focuses on local motions. Supervised optical flow estimation is also biologically implausible. The focus of this paper is on V1 modeling instead of optical flows.

5.4 Unsupervised learning

Assume there is a dataset of frame sequences, where the ground truth displacement fields are unknown. We can learn the model by the following steps: (1) first we take the frames as static images and use the self-supervised learning to initialize the model; (2) then we infer the displacement fields between adjacent pair of frames as the initialization; (3) using adjacent pair of frames as training data, we alternatively update the model parameters and re-infer displacement fields. In this task, we use the parametric M and infer the displacement field by gradient descent on a weighted sum of $\sum_x L_{1,x}(\delta(x))$ and $\|\nabla\delta(x)\|^2$. At each iteration, we start the inference from the inferred displacement field from the last iteration.

We test the unsupervised learning on 200 video sequences sampled from MUG Facial Expression dataset [2]. Since the image size reduces to 64, we use kernel size 8 with a sub-sampling rate of 4 pixels. In the self-supervised learning, we set the range of displacement to $[-3, +3]$. Displacements at image border are leaved out. Figure 5 shows some examples of inferred displacement fields by the unsupervised learning. The inference results are reasonable, which capture the motions around eyes, eyebrows, chin or mouth. See appendix 7.3 for the learned filters.

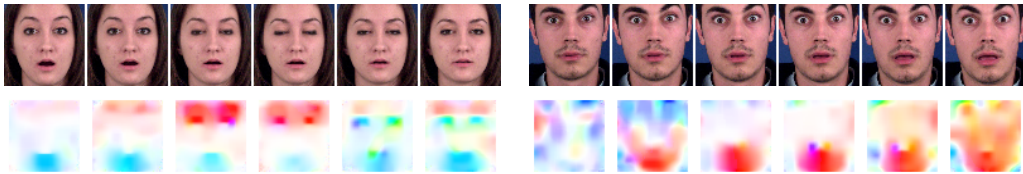


Figure 5: Examples of inferred displacement fields by unsupervised learning. The top row shows the observed image sequences, while the bottom row shows the inferred color coded displacement field [19].

In the appendix, we show more experiment results, including multi-step frame animation (appendix 7.5) and frame interpolation (appendix 7.6), in addition to results mentioned above.

6 Conclusion

This paper proposes a simple representational model for V1 that couples vector representations of local image contents and matrix representations of local motions. Unlike existing models for V1 that focus on statistical properties of natural images or videos, our model serves a direct purpose of perception of local motions caused by the relative motion between the agent and the 3D environment. Our model learns Gabor-like units with quadrature phases. We also give biological interpretations of the learned model and connect it to the spatiotemporal energy model. Our model is novel, and it is our hope that it provides a new mathematical and computational framework for understanding V1.

Project page

<http://www.stat.ucla.edu/~ruiqigao/v1/main.html>

Acknowledgements

The work is supported by DARPA XAI project N66001-17-2-4029; ARO project W911NF1810296; ONR MURI project N00014-16-1-2007; and a Hikvision gift to UCLA. We thank Siyuan Huang for his assistance. We thank Prof. Terrence Sejnowski for helpful discussion. We gratefully acknowledge the support of NVIDIA Corporation with the donation of the Titan Xp GPU used for this research.

References

- [1] Edward H Adelson and James R Bergen. Spatiotemporal energy models for the perception of motion. *Josa a*, 2(2):284–299, 1985.
- [2] Niki Aifanti, Christos Papachristou, and Anastasios Delopoulos. The mug facial expression database. In *11th International Workshop on Image Analysis for Multimedia Interactive Services WIAMIS 10*, pages 1–4. IEEE, 2010.
- [3] Anthony J Bell and Terrence J Sejnowski. The independent components of natural scenes are edge filters. *Vision research*, 37(23):3327–3338, 1997.
- [4] D. J. Butler, J. Wulff, G. B. Stanley, and M. J. Black. A naturalistic open source movie for optical flow evaluation. In A. Fitzgibbon et al. (Eds.), editor, *European Conf. on Computer Vision (ECCV)*, Part IV, LNCS 7577, pages 611–625. Springer-Verlag, October 2012.
- [5] John G Daugman. Uncertainty relation for resolution in space, spatial frequency, and orientation optimized by two-dimensional visual cortical filters. *JOSA A*, 2(7):1160–1169, 1985.
- [6] A. Dosovitskiy, P. Fischer, E. Ilg, P. Häusser, C. Hazırbaş, V. Golkov, P. v.d. Smagt, D. Cremers, and T. Brox. FlowNet: Learning optical flow with convolutional networks. In *IEEE International Conference on Computer Vision (ICCV)*, 2015.
- [7] Robert C Emerson and Morgan C Huang. Quadrature subunits in directionally selective simple cells: counterphase and drifting grating responses. *Visual neuroscience*, 14(2):373–385, 1997.
- [8] KH Foster, James P Gaska, M Nagler, and DA Pollen. Spatial and temporal frequency selectivity of neurones in visual cortical areas v1 and v2 of the macaque monkey. *The Journal of physiology*, 365(1):331–363, 1985.
- [9] Andreas Geiger, Philip Lenz, and Raquel Urtasun. Are we ready for autonomous driving? the kitti vision benchmark suite. In *2012 IEEE Conference on Computer Vision and Pattern Recognition*, pages 3354–3361. IEEE, 2012.
- [10] David H Hubel and Torsten N Wiesel. Receptive fields of single neurones in the cat’s striate cortex. *The Journal of physiology*, 148(3):574–591, 1959.
- [11] Aapo Hyvärinen, Jarmo Hurri, and Jaakko Väyrynen. Bubbles: a unifying framework for low-level statistical properties of natural image sequences. *JOSA A*, 20(7):1237–1252, 2003.
- [12] Aapo Hyvärinen, Juha Karhunen, and Erkki Oja. *Independent component analysis*, volume 46. John Wiley & Sons, 2004.
- [13] E. Ilg, N. Mayer, T. Saikia, M. Keuper, A. Dosovitskiy, and T. Brox. FlowNet 2.0: Evolution of optical flow estimation with deep networks. In *IEEE Conference on Computer Vision and Pattern Recognition (CVPR)*, Jul 2017.
- [14] Naoum P Issa, Christopher Trepel, and Michael P Stryker. Spatial frequency maps in cat visual cortex. *Journal of Neuroscience*, 20(22):8504–8514, 2000.
- [15] Max Jaderberg, Karen Simonyan, Andrew Zisserman, et al. Spatial transformer networks. In *Advances in neural information processing systems*, pages 2017–2025, 2015.
- [16] Judson P Jones and Larry A Palmer. An evaluation of the two-dimensional gabor filter model of simple receptive fields in cat striate cortex. *Journal of neurophysiology*, 58(6):1233–1258, 1987.

- [17] Diederik P Kingma and Jimmy Ba. Adam: A method for stochastic optimization. *arXiv preprint arXiv:1412.6980*, 2014.
- [18] Michael S Lewicki and Bruno A Olshausen. Probabilistic framework for the adaptation and comparison of image codes. *JOSA A*, 16(7):1587–1601, 1999.
- [19] Ce Liu, Jenny Yuen, and Antonio Torralba. Sift flow: Dense correspondence across scenes and its applications. *IEEE transactions on pattern analysis and machine intelligence*, 33(5):978–994, 2010.
- [20] Nikolaus Mayer, Eddy Ilg, Philip Hausser, Philipp Fischer, Daniel Cremers, Alexey Dosovitskiy, and Thomas Brox. A large dataset to train convolutional networks for disparity, optical flow, and scene flow estimation. In *Proceedings of the IEEE Conference on Computer Vision and Pattern Recognition*, pages 4040–4048, 2016.
- [21] Bruno A Olshausen. Learning sparse, overcomplete representations of time-varying natural images. In *Image Processing, 2003. ICIIP 2003. Proceedings. 2003 International Conference on*, volume 1, pages I–41. IEEE, 2003.
- [22] Bruno A Olshausen and David J Field. Emergence of simple-cell receptive field properties by learning a sparse code for natural images. *Nature*, 381(6583):607, 1996.
- [23] Bruno A Olshausen and David J Field. Sparse coding with an overcomplete basis set: A strategy employed by v1? *Vision Research*, 37(23):3311–3325, 1997.
- [24] Marius Pachitariu and Maneesh Sahani. Visual motion computation in recurrent neural networks. *bioRxiv*, page 099101, 2017.
- [25] Daniel A Pollen and Steven F Ronner. Phase relationships between adjacent simple cells in the visual cortex. *Science*, 212(4501):1409–1411, 1981.
- [26] Martin Rehn and Friedrich T Sommer. A network that uses few active neurones to code visual input predicts the diverse shapes of cortical receptive fields. *Journal of computational neuroscience*, 22(2):135–146, 2007.
- [27] Dario L Ringach. Spatial structure and symmetry of simple-cell receptive fields in macaque primary visual cortex. *Journal of neurophysiology*, 88(1):455–463, 2002.
- [28] Jitendra Sharma, Alessandra Angelucci, and Mriganka Sur. Induction of visual orientation modules in auditory cortex. *Nature*, 404(6780):841, 2000.
- [29] Yosef Singer, Yayoi Teramoto, Ben DB Willmore, Jan WH Schnupp, Andrew J King, and Nicol S Harper. Sensory cortex is optimized for prediction of future input. *eLife*, 7:e31557, 2018.
- [30] J Hans van Hateren and Dan L Ruderman. Independent component analysis of natural image sequences yields spatio-temporal filters similar to simple cells in primary visual cortex. *Proceedings of the Royal Society of London B: Biological Sciences*, 265(1412):2315–2320, 1998.
- [31] Laurenz Wiskott and Terrence J Sejnowski. Slow feature analysis: Unsupervised learning of invariances. *Neural computation*, 14(4):715–770, 2002.
- [32] Bolei Zhou, Aditya Khosla, Agata Lapedriza, Antonio Torralba, and Aude Oliva. Places: An image database for deep scene understanding. *arXiv preprint arXiv:1610.02055*, 2016.

7 Appendix

7.1 Animation of learned units: moving V1-like units

We have $M^{(k)}(\delta)v_t^{(k)}(x) = M^{(k)}(\delta)W^{(k)}\mathbf{I}[x]$, where each row of the encoding matrix $W^{(k)}$ serves as a filter. Let $W^{(k)}(\delta) = M^{(k)}(\delta)W^{(k)}$. By changing values of δ , we can animate $W^{(k)}$ to make it move. Each frame shows $(W^{(k)}(\delta), k = 1, \dots, K)$ for a fixed δ . Each block shows the units in the same $W^{(k)}(\delta)$. As δ changes, the orientations of learned units remain the same, while the phases change, and the units belonging to the same sub-vector tend to have similar movements. Please refer to the project page for the animation: <http://www.stat.ucla.edu/~ruiqigao/v1/main.html>.

7.2 Color code of displacement field

Figure 6 shows the color map for the color coded displacement fields used in this paper [19].

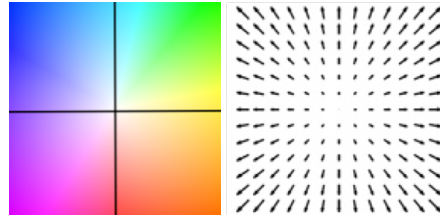


Figure 6: Color map for the color coded displacement fields. The displacement of every pixel in this map is the vector from the center of the square to this pixel. The center pixel does not move. The range of color is taken according to the maximum length of flows in each displacement field.

7.3 Learned filters

Figure 7 shows the learned filters under different settings.

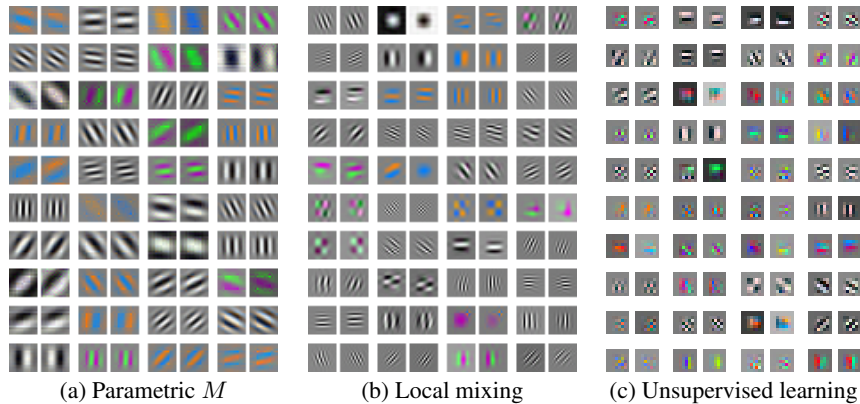


Figure 7: Filters learned from under different settings: (a) filters learned with parametric M ; (b) filters learned with non-parametric M and local mixing motion model (model used in section 5.3); (c) filters learned on MUG Facial expression dataset with unsupervised learning (model used in section 5.4).

Figure 8 shows the learned filters with higher dimensions of sub-vectors (e.g. 4 or 6). Within each block, the orientations of learned patterns tend to be similar but the phases are different, which may be related to the orientation columns in V1 [10, 28]. For fair comparison, we fix the total number of units in the whole vector to 96, and change the number of units in each sub-vector.

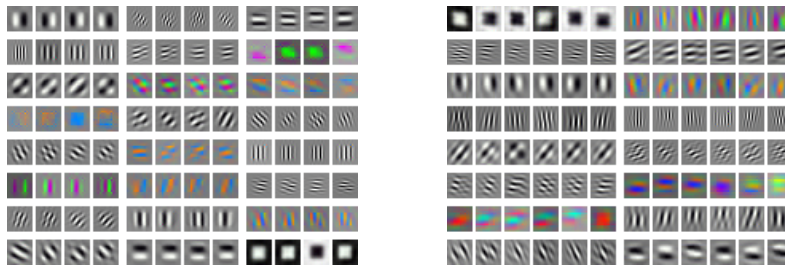


Figure 8: Filters learned with higher dimension of sub-vectors. The total number of units in the whole vector is fixed to 96. Each block shows the learned units within the same sub-vectors.

7.4 Inference of displacement field: qualitative comparison with baseline methods

In figure 9, we show the inference results of displacement fields, together with the results derived by two baseline methods: FlowNet-CS (FNCS) [6] and FlowNet2.0 (FN2) [13].

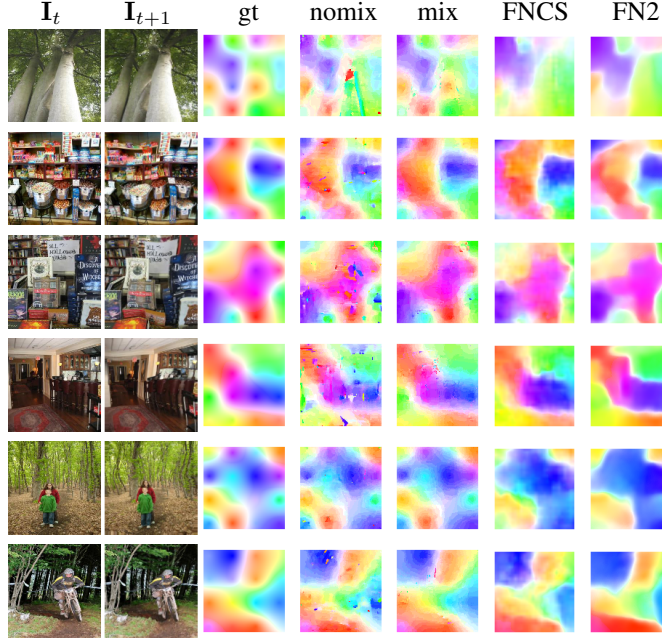


Figure 9: Examples of inference of displacement field. For each line, from left to right are \mathbf{I}_t , \mathbf{I}_{t+1} , ground truth displacement field, inferred displacement field with the original motion model, the local mixing motion model, FNCS and FN2 (FN stands for FlowNet). The displacement fields are color coded. See section ?? for the color map.

7.5 Multi-step frame animation

Given the starting frame $\mathbf{I}_0(x)$ and a sequence of displacement fields $\{\delta_1(x), \dots, \delta_T(x), \forall x\}$, we can animate the subsequent multiple frames $\{\mathbf{I}_1(x), \dots, \mathbf{I}_T(x)\}$ using the learned model. We use the generalized motion model with local mixing generalization, where the local support \mathcal{S} is in a range of $[-4, +4]$, and dx is taken with a sub-sampling rate of 2. We introduce a re-encoding process when performing multi-step animation. At time t , after we get the next animated frame \mathbf{I}_{t+1} , we take it as the observed frame at time $t + 1$, and re-encode it to obtain the latent vector v_{t+1} at time $t + 1$.

We randomly select 1000 testing images that are not observed during training from MIT places365 [32], and for each testing image, randomly generate the displacement fields for 6 steps. Figure 10 displays several examples of the 6-step animation, learned with non-parametric version of M . The animated frames match the ground truth frames well. As a quantitative evaluation, we compute the per pixel distance between the predicted frames and observed frames, which is 9.032 in the testing dataset.

7.6 Frame interpolation

Inspired by the animation and inference results, we show that our model can also perform frame interpolation. Specifically, given a pair of starting frame \mathbf{I}_0 and end frame \mathbf{I}_T , we want to derive a sequence of frames $(\mathbf{I}_0, \mathbf{I}_1, \dots, \mathbf{I}_{T-1}, \mathbf{I}_T)$ that changes smoothly. Let $v_0(x) = W\mathbf{I}_0[x]$ and $v_T(x) = W\mathbf{I}_T[x]$ for each $x \in D$. At time step $t + 1$, like the inference, we can compute $\hat{v}_{t+1}^{(k)}(x, \delta) = \sum_{dx \in \mathcal{S}} M^{(k)}(\delta, dx)v_t^{(k)}(x + dx)$ (we use local mixing motion model) for all possible $\delta \in \Delta$ for all

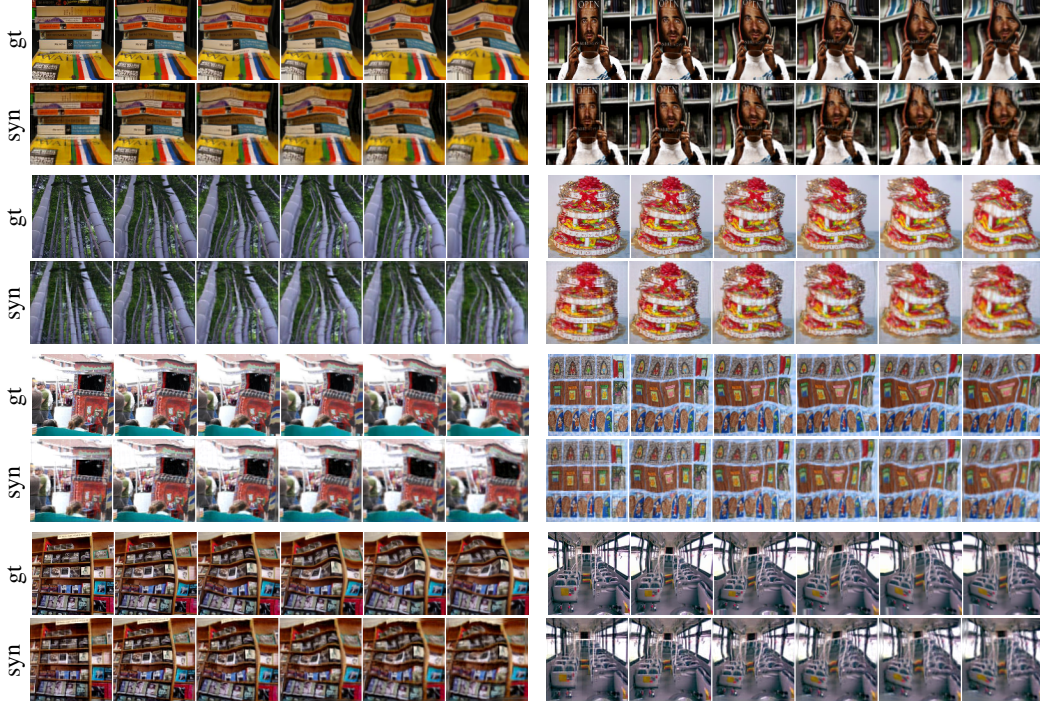


Figure 10: Examples of multi-step animation, learned with non-parametric version of M . For each block, the first row shows the ground truth frame sequences, while the second row shows the animated frame sequences.

$x \in D$ in parallel, and then the algorithm iterates

$$\delta_{t+1}(x) = \arg \min_{\delta \in \Delta} \sum_{k=1}^K \left\| v_T^{(k)} - \hat{v}_{t+1}^{(k)}(x, \delta) \right\|^2, \forall x \in D \quad (10)$$

$$\mathbf{I}_{t+1} = \sum_{x \in D_-} W^\top \hat{v}_{t+1}^{(k)}(x, \delta_{t+1}(x)), \quad (11)$$

$$v_{t+1}(x) = W \mathbf{I}_{t+1}[x], \forall x \in D. \quad (12)$$

We generate pair of frames $(\mathbf{I}_0, \mathbf{I}_T)$ by sampling large displacement on the control points, with range of $[-30, -20] \cup [+20, +30]$. The algorithm stops when \mathbf{I}_t is close enough to \mathbf{I}_T (mean pixel error < 10). Figure 11 shows several examples, learned with non-parametric M . For 96.0% of the testing pairs, the algorithm can accomplish the frame interpolation within 10 steps. With this algorithm, we are also able to infer displacements larger than the acceptable range of δ .

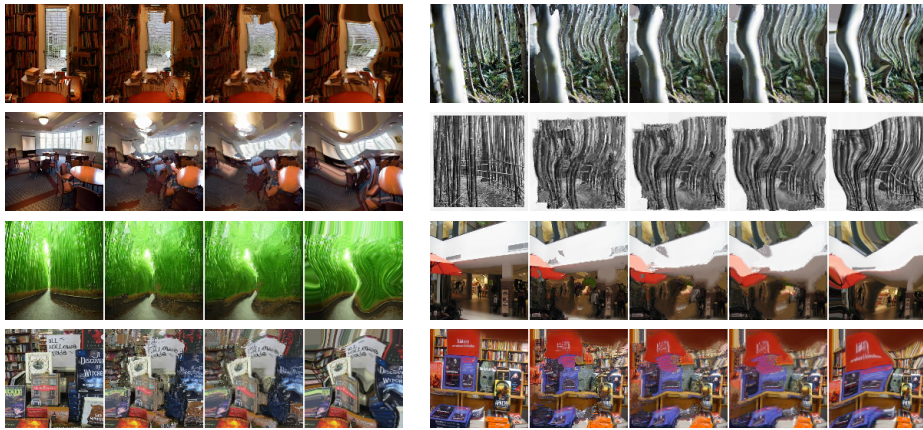


Figure 11: Examples of frame interpolation, learned with non-parametric M . For each block, the first frame and last frame are given, while the frames between them are interpolated frames.